Machine Learning-Based Shear Optimal Adhesive Microstructures with Experimental Validation

Cem Balda Dayan, Donghoon Son, Amirreza Aghakhani, Yingdan Wu, Sinan Ozgun Demir, and Metin Sitti*

Bioinspired fibrillar structures are promising for a wide range of disruptive adhesive applications. Especially micro/nanofibrillar structures on gecko toes can have strong and controllable adhesion and shear on a wide range of surfaces with residual-free, repeatable, self-cleaning, and other unique features. Synthetic dry fibrillar adhesives inspired by such biological fibrils are optimized in different aspects to increase their performance. Previous fibril designs for shear optimization are limited by predefined standard shapes in a narrow range primarily based on human intuition, which restricts their maximum performance. This study combines the machine learning-based optimization and finite-element-method-based shear mechanics simulations to find shear-optimized fibril designs automatically. In addition, fabrication limitations are integrated into the simulations to have more experimentally relevant results. The computationally discovered shear-optimized structures are fabricated, experimentally validated, and compared with the simulations. The results show that the computed shear-optimized fibrils perform better than the predefined standard fibril designs. This design optimization method can be used in future real-world shear-based gripping or nonslip surface applications, such as robotic pick-and-place grippers, climbing robots, gloves, electronic devices, and medical and wearable devices.

C. B. Dayan, D. Son, A. Aghakhani, Y. Wu, S. O. Demir, M. Sitti
Physical Intelligence Department
Max Planck Institute for Intelligent Systems
70569 Stuttgart, Germany
E-mail: sitti@is.mpg.de
M. Sitti
Institute for Biomedical Engineering
ETH Zürich
Zürich 8092, Switzerland
M. Sitti
School of Medicine and College of Engineering
Koç University
Istanbul 34450, Turkey

1. Introduction

Geckos have hairy micro/nanostructures on their toes to stick to diverse surfaces. These fibril adhesives have some branches and hierarchical structures called setae. Their geometry is highly complex with spatula and mushroom tip endings.[1] Such fibrillar adhesives give highly repeatable and controlled adhesion with no residual remaining on the contact surface.[2] These advantages come from the source of the adhesion, which is intermolecular interactions, such as van der Waals forces.[3,4] Such fibrillar adhesives are also investigated for their self-cleaning,[5–8] contact mechanics,[9,10] liquid repellency,[11,12] shear,[13–15] and adhesion under different environmental conditions.[16] These advantages have inspired many studies to fabricate synthetic bioinspired fibrillar adhesives for various applications.[11,13,17] In some cases, synthetic adhesives performed even better than their biological counterparts on smooth surfaces.[18,19]

Many studies have investigated bioinspired nondirectional vertical fibrillar adhesives with various geometries and materials.[1] Most studies have focused on maximizing the adhesion of these synthetic fibrillar adhesives using both analytical and advanced computational methods as a function of fiber stem and tip ending shape, fiber placement, spacing, and material properties. Mushroom/wedge-shaped,[20] T-shaped[21–23] and 3D designed[24,25] fibrils have shown the most enhanced adhesion. However, the maximized shear of these fibrils has not been investigated yet using advanced computational methods. The fibril structures should initially have high contact area and adhesion with the contact surface to obtain high shear.[26] During shear, mushroom-shaped fibrils bend after a certain critical point and carry normal and shear stress on the tip of the fibril's circumference, and, as a result, the actual contact area decreases. It causes a reduction in shear force. Therefore, the 3D shape of the fibril stem and tip ending needs to be optimized for maximum shear.

Machine learning methods have been implemented in many different fields for optimizing the 3D design of structures in buildings,[27] ships,[28] aircraft,[29] antennae,[30] and materials.[31,32] Most of these optimizations used neural networks

**ADVANCED
SCIENCE NEWS**

www.advancedsciencenews.com

**NANO · MICRO
small**

www.small-journal.com

or genetic algorithms. However, these approaches have significant disadvantages in requiring an extensive training data set with more computational time. There are more time-effective alternatives for machine-learning-based design optimization, such as the Bayesian optimization. Moreover, these optimizations can be implemented in fibril adhesive designs as in previous studies for maximizing their adhesion.[24,25] However, no one has investigated shear-optimal 3D fibril designs using machine-learning approaches yet.

Developing nondirectional shear optimal microstructures are important to advance many fields and applications requiring high shear forces, such as climbing robots, robotic grippers, and surgical robot graspers. Climbing robots need high shear capability on their contact surfaces to avoid any possible slipping to improve their locomotion and even make it possible to climb high-angle inclined surfaces.[33] Otherwise, their performance will be limited to several tasks only. As another example, for robotic grippers, since aimed gripping item shapes are usually uncertain in real-life, one of the biggest challenges is holding large-curvature objects without over-squeezing them but still being able to grip them.[34] To solve this challenge, gripper holders should have high-shear performance surfaces to hold the objects with much less required squeezing pressure while grasping. Developing high-shear performance microstructures is critical for improving the current performance of robotic grippers, especially for fragile items that cannot resist high-pressing forces. Another crucial field that potentially benefits from developing shear-optimal microstructures is surgical robot graspers. In some medical operations, grasping a tissue is essential to be able to do the tasks with surgical robot graspers. However, these graspers should hold the tissue without causing any damage.[35,36] This ability is only possible by having an interfacial layer between the grasper surface and tissue. Due to that, the high-performing shear optimal microstructures can be decorated on a grasper surface to hold the tissue. It will also decrease the required pressing forces dramatically. In the end, the operation can be conducted to decrease the possible damage to a patient's tissue. It will decrease the possible trauma in the operation region dramatically. In addition to all these advantages, developing high-performance shear optimal microstructures will not leave any residual to contact surfaces.

Previous studies used predefined limited fibril shapes to investigate their shear performance. A more general approach is needed to reduce these limitations and explore more optimal fibril shapes with higher shear performance. Therefore, we propose a machine learning-based optimization method using finite element methods (FEM)-based shear modeling to optimize the shear of 3D fibril designs. We fabricated such 3D fibril designs using two-photon polymerization (2PP) technique to validate them experimentally. This method provides the advantage of searching a vast design space relatively faster than trial-error and other optimization methods.[37] In addition, the implemented Bayesian optimization framework is highly data-efficient, and the optimization framework requires 300 iteration runs for each design to find the optimal fibril design. Moreover, the Bezier-curve-based body shape computational modeling gives high flexibility for investigating the optimal fibril design compared to standard predefined shapes. In each iteration, the shear results are estimated with the FEM simulations, and the Bayesian optimizer suggests another fibril design according to the FEM-estimated

results. The proposed framework saves reasonable time during shear-optimal fibril design investigation, and it finds the optimal shape for defined tip diameter and aspect ratio (AR) in ≈5 h in our system. Finally, the optimal fibril shapes are experimentally validated.

2. Results

FEM-based shear simulation and the Bayesian optimization are the two main parts of the proposed shear optimization framework (**Figure 1**a). FEM simulation was used for shear force estimation, and the Bayesian optimization was used for investigating the optimal estimated design. In each iteration, the Bayesian optimization suggested design parameters to evaluate the estimated shear for the simulation. This process continued until the iteration limit (300 iterations) was achieved, which gave us the optimal fibril design (Figure S1, Supporting Information).

The FEM simulation was built in 2D for all shapes. The contact surface was assumed as smooth and locally flat. The side profile of the 3D fibril was modeled using a Bezier curve. Three different ARs (1, 0.6, 0.4) and three different tip diameters (40, 60, and 80 μm) were considered to explore the fibril size effects. In addition to that 2PP-based 3D fibril fabrication limitation, such as the minimum achievable fillet radius of 2.7 μm at the tip of the fibrils, was integrated into the simulations.

The shear performance of a fibril was simulated with its deformation using the Mooney–Rivlin hyperelastic model.[38,39] During the simulations, the shear force of the fibril was calculated by integrating the shear stress on the fibril tip line. After taking the line integral, the unit force was divided by the measured tip diameter of the fibril and multiplied by the tip area of the fibril. This way, we obtained the equivalent shear force from the 2D FEM simulation. In the simulations, it was assumed that the fibril tip had contact with a smooth and locally flat surface. Initially, all the fibrils were compressed with a locally flat probe with a constant preload pressure of ≈600 kPa. After compression, the fibril base was moved to the right side with small step sizes to create shear on the fibril. During measurements, first, the applied preload is reached and waited until the end of preload duration, and then, the shear begins. During shear measurement, there was no feedback mechanism to keep the applied normal pressure constant at the same value; instead, the z-position is kept fixed throughout experiments. During the shear, if the interfacial critical normal stress value[40,41] was reached on any region of the fibril's tip surface, then the simulation assumed that the fibril detached from the surface.

As an optimizer, the Bayesian optimization method was used and connected to the FEM simulation. One of the main advantages of this method was keeping the iteration number as low as possible. This optimization method could help decrease the number of simulation runs and increase our approach's efficiency. The fixed parameters were the minimum fillet radius due to the fibril fabrication limitations, the fibril tip diameter, and the fibril stem height for corresponding categories. In each iteration, the optimization framework considered the Bezier-curve control points as optimizable variables and suggested the optimal design (Figure 1b). Our method aimed to maximize the shear force. Here, all of the fibril designs were directly fabricated by a 2PP process with an elastomeric resin material (Figure 1c,d). Before
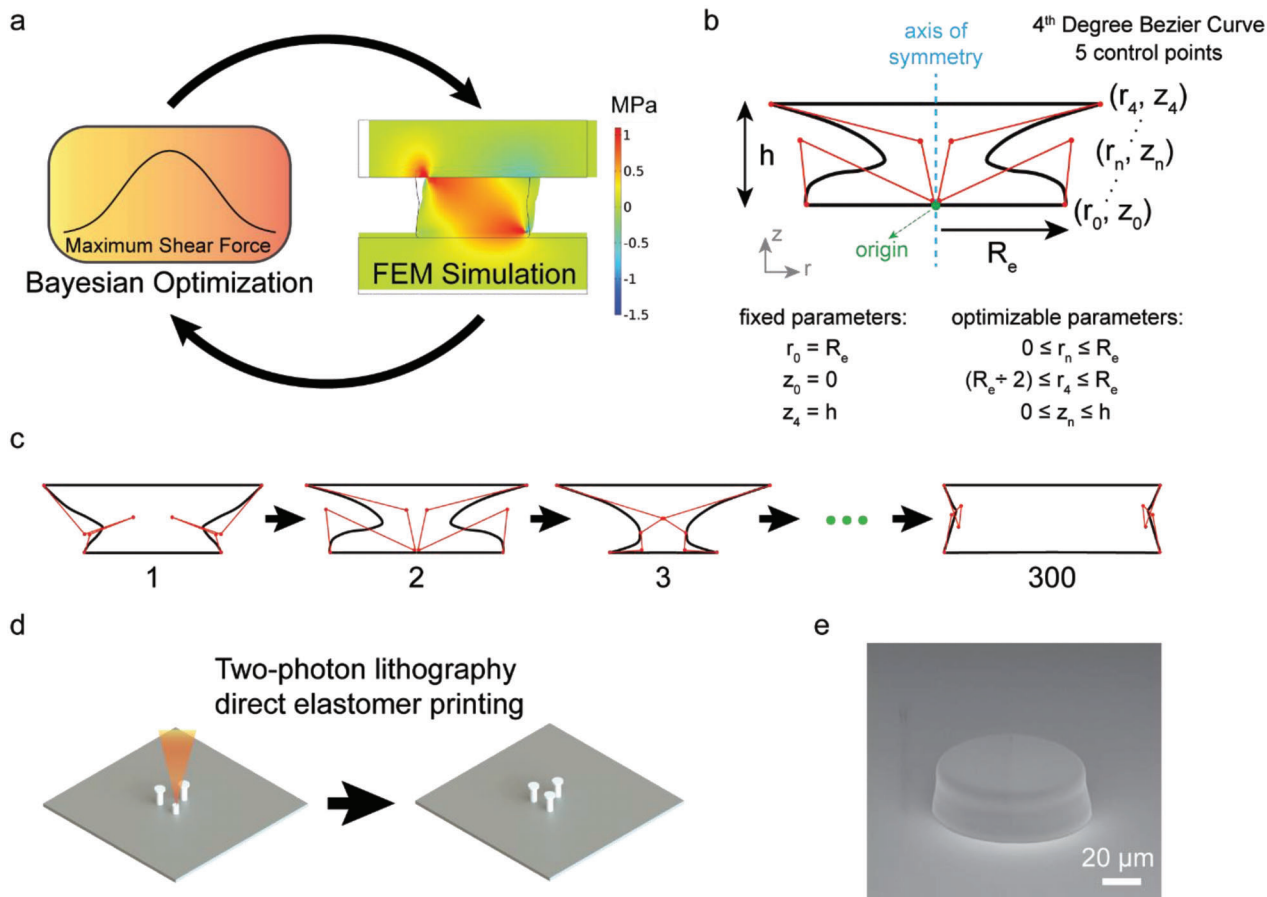
**ADVANCED
SCIENCE NEWS**

www.advancedsciencenews.com

NANO · MICRO

small

www.small-journal.com

Figure 1. Overall summary for investigating the Bayesian optimization-based shear-optimized microfibril designs. a) Optimization framework for investigating the machine learning-based (ML-based) optimal microfibril designs. b) Design parameters of a fibril for Bayesian optimization. c) Starting from a random shape, the fibril design changes in each iteration until obtaining the maximum shear force. d) Fabrication procedure of the optimal fibrils using two-photon lithography technique using an elastomeric resin material. e) Scanning electron microscope (SEM) image of a sample fabricated optimal microfibril with an 80 μm tip diameter and 0.4 AR.

starting the optimization process, the essential parameters were experimentally measured and included in the simulations, such as the hyperelastic model parameters, the minimum fillet radius due to fabrication limitations, and the interfacial critical normal stress.

During shear, the interfacial stress of the optimal fibril showed that the stress distributions were changing along the fibril tip contact surface area (**Figure 2**). The normal stress distribution of the fibril showed that the opposite side of the shear direction of the fibril edge's interfacial stress distribution increased during shear. After reaching the critical interfacial normal stress, the opposite side of the shear direction of the fibril edge's interfacial stress distribution was assumed to be detached from the surface. As a result, the detachment started from the critical interfacial normal stress-reached part of the fibril and continued as a crack propagation to the other end of the fibril (Figure 2a–c). During shear, the interfacial shear stress distribution of the fibril also changed. The shear stress values increased along the fibril interface during shear. Especially, both ends of the fibril's interfacial stress values increased drastically (Figure 2d–f).

The optimized fibrils with various tip diameters and ARs were found with the proposed optimization framework. The fibrils' three different tip diameters (40, 60, and 80 μm) were optimized for three different ARs (1, 0.6, and 0.4). All of the nine optimal fibril designs are shown in **Figure 3**. For high aspect ratio (AR 1) fibril designs, the stiffness of the fibrils was tried to be increased by maximizing the values of the Bezier curve control points to obtain higher shear force.

The shear performance of the fabricated optimal fibrils was characterized by a hemispherical-smooth glass probe with a 10 mm diameter. Since the tip diameters of the fibrils were much smaller than the smooth glass probe, flat-flat contact geometry can be assumed between the fibrils and the contact probe during measurements. All 40 μm tip diameter fibril designs were printed as a tripod with three structures for measurements. The rest of the tip diameter designs (60 and 80 μm) were fabricated as a single structure. Standard shapes (flat-punch and wedge-shaped mushroom fibrils) were also fabricated and considered as a control in this study. These structures were widely known and commonly used in the literature for high adhesion and shear.
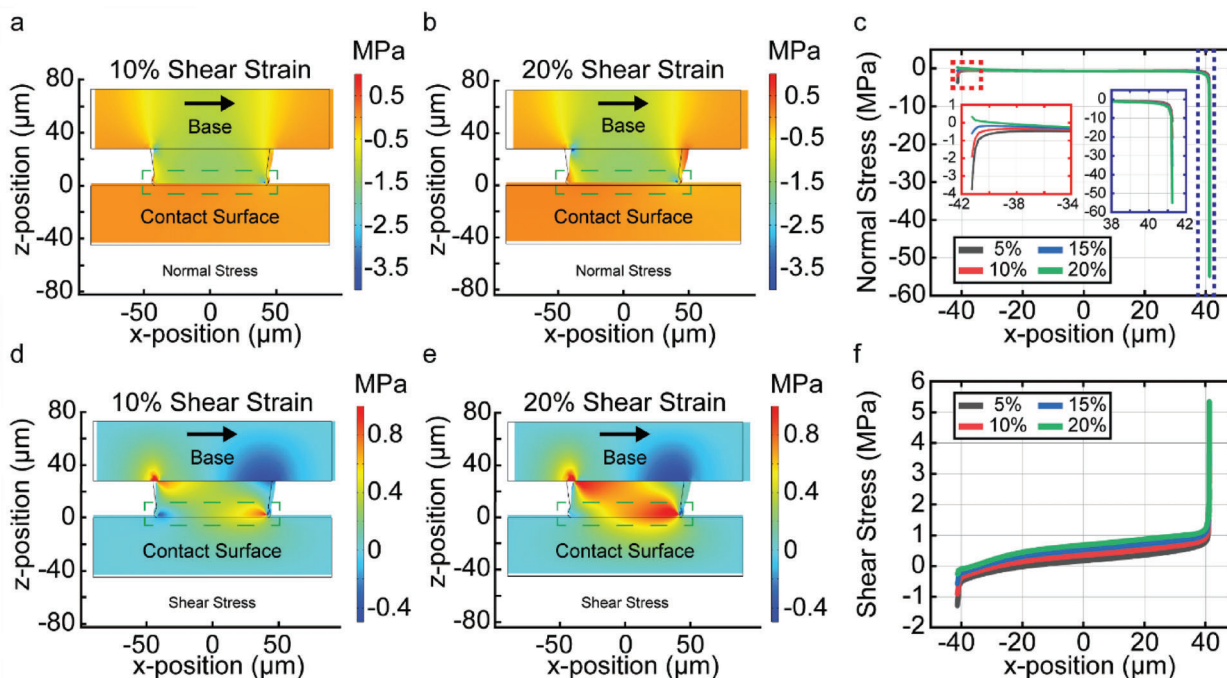
ADVANCED
SCIENCE NEWS

www.advancedsciencenews.com

NANO · MICRO

small

www.small-journal.com

Figure 2. Normal and shear stress distribution under different shear strains for an 80 μm tip diameter and AR 0.4 ML-found optimal design. Normal stress distribution a) under 10% shear strain, b) under 20% shear strain, c) on a tip-contact surface interface for four different shear strains (5%, 10%, 15%, 20%) for 80 μm tip diameter and AR 0.4 ML-found optimal design are shown, respectively. Shear stress distribution d) under 10% shear strain, e) under 20% shear strain, f) on a tip-contact surface interface for four different shear strains (5%, 10%, 15%, 20%) for 80 μm tip diameter and AR 0.4 ML-found optimal design are shown, respectively. The dashed green rectangular area encloses the interested stress distribution line between the fibril tip and the contact surface.
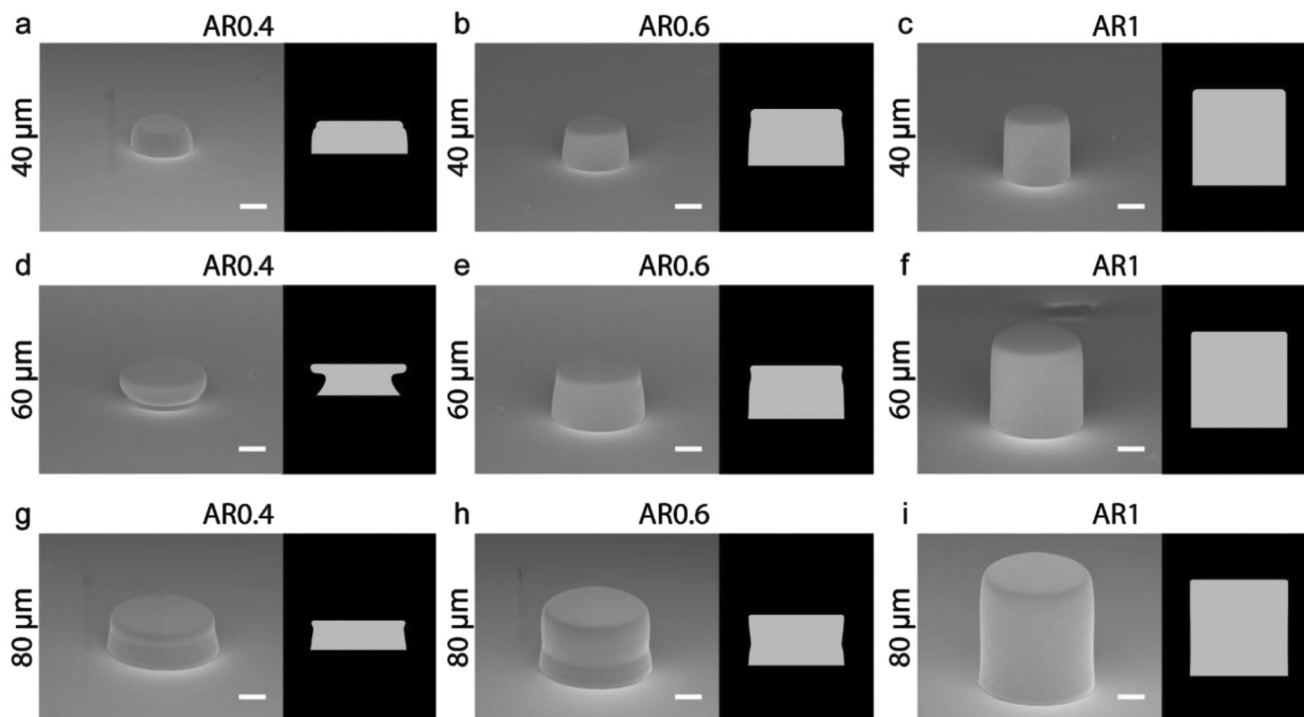

Figure 3. SEM images of the fabricated ML-found optimal elastomeric fibril structures for three different tip diameters (40, 60, and 80 μm) and three different ARs (0.4, 0.6, and 1). The tip diameter 40, 60, and 80 μm designs are (a–c), (d–f), (g–i), respectively. The AR 0.4, 0.6, and 1 designs are (a,d,g), (b,e,h), (c,f,i), respectively. All scale bars are 20 μm.
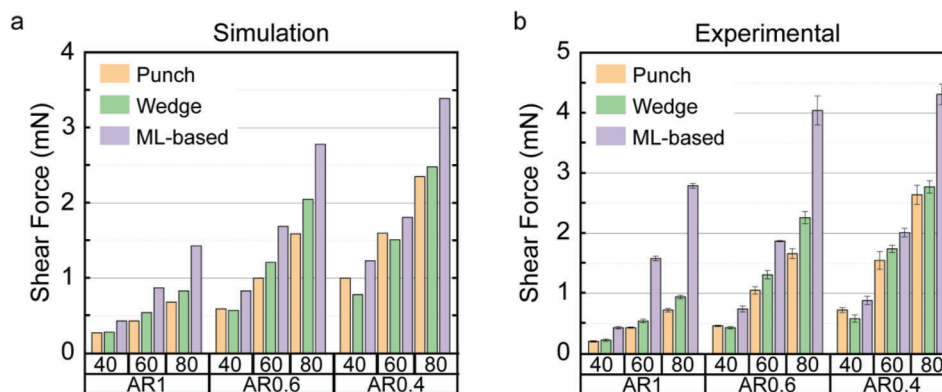
ADVANCED
SCIENCE NEWS
www.advancedsciencenews.com

NANO · MICRO
small
www.small-journal.com

Figure 4. Shear results in FEM simulations and experiments for a single fibril using a flat punch, wedge-shaped, and ML-based optimal designs. a) The FEM simulation results show that ML-based optimal designs have better shear performance than the standard flat punch and wedge-shaped fibril designs. b) The experimental results agree with the FEM simulation results, proving that the ML-found designs give higher shear forces than the standard shapes in all cases.

Shear performance comparison among all possible fibril designs is shown in **Figure 4** with experimental and simulation results. Machine learning-based optimal fibril designs performed better than the standard shapes in simulations and experiments in all cases. Moreover, the predicted shear forces show agreement with the experiments in all fibril designs and categories. The results show that if the fibril's tip diameter increases, the fibril's shear force also increases for a single structure. This phenomenon also applies to the AR. If the AR decreases, the fibril's shear force increases for a single fibril. This trend is related to the stiffness of the fibrils. If the stiffness of the fibril rises, then its shear performance also increases. However, there should be a limit to increasing the stiffness of the structures. If the stiffness of the made of material of the fibrils increases, then after a certain point, the conformal contact between the fibril tips and the contact surface worsens, which would reduce the shear performance.

3. Conclusion

Our approach for investigating shear-optimal fibril designs with experimental validation could compute shear-optimal fibril designs accurately and efficiently. This investigation is possible by linking the FEM shear simulation with the Bayesian optimization method instead of designing fibrils based on human intuition or analytical models. The computational machine learning approach enables us to efficiently explore a broad range of fibril designs to maximize the shear performance. Additionally, the Bezier-curve-based fibril body design gives significant flexibility to investigate broad fibril designs. Besides the simulation results, experimental results have validated the computed shear-optimal fibril designs. Furthermore, the ML-found shear optimal structures were compared with the work of other researchers in this study. Therefore, the shapes of the other researchers (wedge mushroom and flat punch) were also included and fabricated with our materials and our fabrication process to compare them fairly with the ML-based optimal structures. Otherwise, the shape effect will not be the only factor due to the other effects of several factors, such as material and fabrication process. Based on this comparison, our ML-based shear optimal structure designs have

better shear performance than the literature's proposed designs. As a future work, fibril designs that optimize adhesion, shear, and wetting can be studied using the given computational framework. Integrated fabrication limitation in simulations makes the FEM simulation environment more realistic than other simulation approaches.[25] As a result, the computed optimal design performances matched well with the experimental ones. These findings are crucial for many real-world shear-dominated fibrillar adhesive applications in robotic grippers for pick-and-place and object manipulation,[42] climbing or other mobile robots that require nonslipping limbs,[43] and biomedical devices to anchor and nonslip on surfaces.[44]

4. Experimental Section

FEM Simulations: For FEM simulations, a commercial FEM software (COMSOL Multiphysics 5.6, COMSOL Inc.) was used. The simulations were used to estimate the shear force of the standard and optimal fibril designs. The fibril base was fixed on the substrate in the simulations, and the top part of the fibril tip ending was in touch with the contact surface. At the beginning of the simulation, the contact surface iteratively translated and compressed the fibril on the z-axis until reaching ≈600 kPa. After that, the fibril substrate moved on the x-axis until the tip of the fibril's stress reached the critical interfacial normal stress. Then, the simulation terminated, and the shear force was calculated. The shear force of the fibril was calculated by integrating the shear stress on the fibril tip line, leading to unit force per length (N m^{-1}). After taking the line integral, the unit force was divided by the measured tip diameter of the fibril and multiplied by the tip area of the fibril, giving the total shear force.

For simulations, some material characterizations have been realized experimentally. Initially, all standard shapes were fabricated by the 2PP method, and commercial IP-PDMS elastomeric resin was used as a material. The SEM images were used for defining the geometrical fabrication limitation: the minimum tip edge fillet radius. For the Mooney–Rivlin two parameters, the normal adhesion measurements were conducted. For finding the critical normal stress values, shear characterizations were realized for all standard fibrils (flat-punch pillar and wedge mushroom).[20] The related fabrication limitations were also included in simulations for standard fibrils. The shear measurements were matched with the shear simulations for all standard shapes and categories (tip diameter and ARs) by minimizing the root-mean-squared relative error to find each AR's critical normal stress. It was found that one specific critical normal stress

**ADVANCED
SCIENCE NEWS**

www.advancedsciencenews.com

**NANO · MICRO
small**

www.small-journal.com

existed for each AR. For ARs 1, 0.6, and 0.4, the critical normal stresses were −264.0, −14.5, and 362.9 kPa, respectively. Since the experimental results were related to the simulation results for standard shapes before starting the exploration of the optimal designs, this approach made the simulation results comparable with the real experiments.

The design of the fibrils included fixed and optimizable parameters. The fixed parameters included the minimum edge fillet radius, tip diameter (for each category), AR (for each category), Mooney–Rivlin parameters, and critical normal stress (for each AR). The optimizable parameters included the 4th degree of Bezier-curve control points with three Bezier-curve control points and a fibril base diameter. More than 10 000 free triangular elements were used as meshes in each 2D simulation. Significantly, the meshes were extremely fine toward the tip of the fibril to catch the critical normal stress for detachment precisely.

Bayesian Optimization: The Bayesian optimization was implemented using a prebuilt function called "bayesopt.m" on MATLAB (MATLAB R2018a, The MathWorks, Inc.). As an acquisition function, expected improvement was used. The number of iterations was set to 300. The Bayesian optimizer (implemented in MATLAB) was linked with COMSOL FEM simulation (COMSOL Multiphysics 5.6, COMSOL Inc.) via LiveLink. The Bayesian optimizer's suggested design was sent to FEM simulation in each iteration. The FEM simulation ran and calculated the estimated shear force. Afterward, the estimated shear force was returned to the Bayesian optimizer to decide which design point should be evaluated next. All process took ≈5 h to find the optimal design for one specific tip diameter and AR. This framework was implemented on a desktop computer that had Intel Xeon CPU with 20 cores (E5-2680 v2, 2.80 GHz), 192 GB RAM, and NVIDIA Quadro K5000 graphics card.

Fibril Fabrication: For each standard and optimal fibril design, the computer-aided design was implemented by Solidworks, and then a stereolithography file (.stl) was created. The generated files were uploaded into the Nanoscribe software (Photonic Professional GT2, Nanoscribe GmbH, Germany). The two-photon lithography system was used in DiLL mode. In this mode, the elastomeric resin material (IP-PDMS, Nanoscribe GmbH, Germany) was placed between the substrate glass and the objective. As the objective lens, 25x, 0.8 NA objective was used. After the printing of desired fibril structures, the post-process was applied. The fabricated fibrils were immersed in a beaker containing isopropyl alcohol (IPA) for 15 min. Next, the samples were immersed in another beaker containing fresh IPA for 2 min. Young's modulus of the material was 15.3 MPa.[45,46] For material behavior on a small scale, a T-shape fibril's stress–strain curve on a smooth spherical glass was used for Mooney–Rivlin's second-order model fitting.[47] The printed T-shape fibril's stress–strain curve was obtained by normal force measurements. The obtained stress–strain curve was used for Mooney–Rivlin's second-order model fitting, withholding the constraints according to the literature.[47] The Mooney–Rivlin parameters were obtained by minimizing the sum square error of the fitting curve with estimation for fibril's experimentally obtained stress–strain curve using the "fmincon.m" function including the required constraints for Mooney–Rivlin parameters in MATLAB (MATLAB R2019a, The MathWorks, Inc.). The computed Mooney–Rivlin second-order model fitting parameters were used in all simulations. These values were $C10 = 1.01e + 6$ Pa and $C01 = 5.96e + 5$ Pa.

Shear and Adhesion Measurements: A custom-made shear-adhesion setup was used for tangential/shear and normal force measurements. A video camera (Grasshopper3, Point Grey Research Inc.) was mounted on an inverted optical microscope (Axio Observer A1, Zeiss) to visualize the measurements. For z-direction and y-direction, a computer-controlled high-precision stage (LPS-65 2″, Physik Instrumente GmbH & Co. KG) was attached to the microscope. Two load cells (y-axis: LSB200, 100 g, JR S-Beam, FUTEK, and z-axis: GSO-25, Transducer Technique LLC) were mounted on the stage in an orientation to measure the forces on the y-axis and z-axis. The motion of the piezo stages was controlled, and a custom-made program processed the data acquisition by a LabVIEW (National Instruments, Austin, TX, USA). A smooth spherical glass probe with a 10 mm diameter was used as a contact surface. The load-drag tests were done for shear. Before applying shear, the normal pressure (≈600 kPa) was exerted on the fibril. After reaching the desired preload, 60 s of relaxation

time waited. Tangential displacement was applied for 1 mm after relaxation time. During the measurements, all speeds (approaching speed on the z-axis, shear speed on the y-axis, and retraction speed on the z-axis) were set to 5 μm s^{-1}. Each measurement was repeated five times.

Supporting Information

Supporting Information is available from the Wiley Online Library or from the author.

Acknowledgements

Conflict of Interest

The authors declare no conflict of interest.

Data Availability Statement

The data that support the findings of this study are available from the corresponding author upon reasonable request.

Keywords

[1] R. D. O'Rorke, T. W. J. Steele, H. K. Taylor, *J. Adhes. Sci. Technol.* **2016**, *30*, 362.

[2] R. Ruibal, V. Ernst, *J. Morphol.* **1965**, *117*, 271.

[3] K. Autumn, M. Sitti, Y. A. Liang, A. M. Peattie, W. R. Hansen, S. Sponberg, T. W. Kenny, R. Fearing, J. N. Israelachvili, R. J. Full, *Proc. Natl. Acad. Sci. U. S. A.* **2002**, *99*, 12252.

[4] K. Autumn, Y. A. Liang, S. T. Hsieh, W. Zesch, W. P. Chan, T. W. Kenny, R. Fearing, R. J. Full, *Nature* **2000**, *405*, 681.

[5] S. Kim, E. Cheung, M. Sitti, *Langmuir* **2009**, *25*, 7196.

[6] Y. Mengüç, M. Röhrig, U. Abusomwan, H. Hölscher, M. Sitti, *J. R. Soc., Interface* **2014**, *11*, 20131205.

[7] G. J. Amador, T. Endlein, M. Sitti, *J. R. Soc., Interface* **2017**, *14*, 20170134.

[8] U. A. Abusomwan, M. Sitti, *Langmuir* **2014**, *30*, 11913.

[9] N. J. Glassmaker, A. Jagota, C. Y. Hui, W. L. Noderer, M. K. Chaudhury, *Proc. Natl. Acad. Sci. U. S. A.* **2007**, *104*, 10786.

[10] H. Gao, H. Yao, *Proc. Natl. Acad. Sci. U. S. A.* **2004**, *101*, 7851.

[11] C. B. Dayan, S. Chun, N. Krishna-Subbaiah, D. M. Drotlef, M. B. Akolpoglu, M. Sitti, *Adv. Mater.* **2021**, *33*, 31.

[12] V. Liimatainen, D. M. Drotlef, D. Son, M. Sitti, *Adv. Mater.* **2020**, *32*, 2000497.

[13] M. P. Murphy, B. Aksak, M. Sitti, *Small* **2009**, *5*, 170.

[14] Y. Mengüç, S. Y. Yang, S. Kim, J. A. Rogers, M. Sitti, *Adv. Funct. Mater.* **2012**, *22*, 1246.

[15] M. Zhou, Y. Tian, D. Sameoto, X. Zhang, Y. Meng, S. Wen, *ACS Appl. Mater. Interfaces* **2013**, *5*, 10137.

[16] C. T. Mitchell, C. B. Dayan, D. M. Drotlef, M. Sitti, A. Y. Stark, *Sci. Rep.* **2020**, *10*, 19748.

[17] M. P. Murphy, S. Kim, M. Sitti, *ACS Appl. Mater. Interfaces* **2009**, *1*, 849.

[18] D.-M. Drotlef, C. B. Dayan, M. Sitti, *Integr. Comp. Biol.* **2019**, *59*, 227.

[19] H. E. Jeong, J.-K. Lee, H. N. Kim, S. H. Moon, K. Y. Suh, *Proc. Natl. Acad. Sci. U. S. A.* **2009**, *106*, 5639.

[20] B. Aksak, K. Sahin, M. Sitti, *Beilstein J. Nanotechnol.* **2014**, *5*, 630.

[21] G. Carbone, E. Pierro, *Small* **2012**, *8*, 1449.

[22] R. G. Balijepalli, M. R. Begley, N. A. Fleck, R. M. McMeeking, E. Arzt, *Int. J. Solids Struct.* **2016**, *85–86*, 160.

[23] G. Carbone, E. Pierro, S. N. Gorb, *Soft Matter* **2011**, *7*, 5545.

[24] D. Son, V. Liimatainen, M. Sitti, *Small* **2021**, *17*, 2102867.

[25] Y. Kim, C. Yang, Y. Kim, G. X. Gu, S. Ryu, *ACS Appl. Mater. Interfaces* **2020**, *12*, 24458.

[26] M. Piccardo, A. Chateauminois, C. Fretigny, N. M. Pugno, M. Sitti, *J. R. Soc., Interface* **2013**, *10*, 20130182.

[27] P. Geyer, S. Singaravel, *Appl. Energy* **2018**, *228*, 1439.

[28] H. Cui, O. Turan, P. Sayer, *Comput.-Aided Des.* **2012**, *44*, 186.

[29] O. Hennigh, in *6th Int. Conf. Learning Representations, ICLR 2018 – Workshop Track Proc.*, OpenReview, Vancouver Convention Center, Vancouver, BC, Canada, **2018**, 1, https://iclr.cc/Conferences/2018.

[30] D. Linden, G. Hornby, A. Globus, in *Automated Antenna Design with Evolutionary Algorithms*, American Institute of Aeronautics and Astronautics, Reston, VA **2006**, p. 7242, https://ntrs.nasa.gov/api/citations/20060024675/downloads/20060024675.pdf.

[31] N. O. Dogan, U. Bozuyuk, P. Erkoc, A. C. Karacakol, A. Cingoz, F. Seker-Polat, M. A. Nazeer, M. Sitti, T. Bagci-Onder, S. Kizilel, *Adv. Nanobiomed Res.* **2022**, *2*, 2100033.

[32] G. Dogan, S. O. Demir, R. Gutzler, H. Gruhn, C. B. Dayan, U. T. Sanli, C. Silber, U. Culha, M. Sitti, G. Schütz, C. Grévent, K. Keskinbora, *ACS Appl. Mater. Interfaces* **2021**, *13*, 54503.

[33] H. K. Raut, A. Baji, H. H. Hariri, H. Parveen, G. S. Soh, H. Y. Low, K. L. Wood, *ACS Appl. Mater. Interfaces* **2018**, *10*, 1288.

[34] E. W. Hawkes, D. L. Christensen, A. K. Han, H. Jiang, M. R. Cutkosky, in *2015 IEEE Int. Conf. Robotics and Automation (ICRA)*, IEEE, Piscataway, NJ **2015**, pp. 2305–2312, http://bdml.stanford.edu/uploads/Profiles/AdhesionPublications/ICRA15Curved.pdf.

[35] I. Waters, L. Wang, D. Jones, A. Alazmani, P. Culmer, *IEEE Sens. J.* **2022**, *22*, 16545.

[36] I. Waters, A. Alazmani, P. Culmer, *IEEE Trans. Med. Robot Bionics* **2020**, *2*, 541.

[37] C. B. Dayan, F. Afghah, B. S. Okan, M. Yıldız, Y. Menceloglu, M. Culha, B. Koc, *Mater. Des.* **2018**, *148*, 87.

[38] M. Mooney, *J. Appl. Phys.* **1940**, *11*, 582.

[39] R. S. Rivlin, *Philos. Trans. R. Soc., A* **1948**, *241*, 379.

[40] B. Aksak, C. Y. Hui, M. Sitti, *J. R. Soc., Interface* **2011**, *8*, 1166.

[41] T. Tang, C. Y. Hui, N. J. Glassmaker, *J. R. Soc., Interface* **2005**, *2*, 505.

[42] A. Koivikko, D.-M. Drotlef, C. B. Dayan, V. Sariola, M. Sitti, *Adv. Intell. Syst.* **2021**, *3*, 2100034.

[43] D. Son, H. Gilbert, M. Sitti, *Soft Rob.* **2020**, *7*, 10.

[44] J. Klein, *Polym. Adv. Technol.* **2012**, *23*, 729.

[45] A.-I. Bunea, N. del Castillo Iniesta, A. Droumpali, A. E. Wetzel, E. Engay, R. Taboryski, *Micro* **2021**, *1*, 164.

[46] P. F. J. van Altena, A. Accardo, *Polymers* **2023**, *15*, 1816.

[47] N. Kumar, V. V. Rao, *MIT Int. J. Mech. Eng.* **2016**, *6*, 43.